

Specification of rain gauge representativity error for data assimilation

Philippe Lopez¹, Geun-Hyeok Ryu²,
Byung-Ju Sohn², Laura Davies³,
Christian Jakob³ and Peter Bauer¹

Research Department

¹ECMWF, Reading, UK

²Seoul National University, South Korea

³Monash University, Melbourne, Australia

To be submitted to Q. J. R. Meteorol. Soc.

June 2011

This paper has not been published and should be regarded as an Internal Report from ECMWF.

Permission to quote from it should be obtained from the ECMWF.



Series: ECMWF Technical Memoranda

A full list of ECMWF Publications can be found on our web site under:

<http://www.ecmwf.int/publications/>

Contact: library@ecmwf.int

©Copyright 2011

European Centre for Medium-Range Weather Forecasts
Shinfield Park, Reading, RG2 9AX, England

Literary and scientific copyrights belong to ECMWF and are reserved in all countries. This publication is not to be reprinted or translated in whole or in part without the written permission of the Director-General. Appropriate non-commercial use will normally be granted under the condition that reference is made to ECMWF.

The information within this publication is given in good faith and considered to be true, but ECMWF accepts no liability for error, omission and for loss or damage arising from its use.

Abstract

The comparison of precipitation fields produced by numerical weather prediction models with rain gauge observations is often difficult because the former are assumed to represent grid box averages, while the latter can be considered as point measurements. Obtaining a reasonable estimate of the representativity error (RE) for rain gauges is a prerequisite to their proper use in model validation and above all in data assimilation.

In this work, RE is evaluated in terms of the spatial variability of precipitation over a typical model grid box. It is also assumed that the total RE of rain gauges can be split into a large-scale and a small-scale contribution. The large-scale component is estimated from various ground-based radar precipitation datasets, while the small-scale component is derived from several high-density rain gauge networks.

A quantitative estimation of RE is obtained for rain rate (RR) as well as for its logarithmic transform ($\ln[RR + 1]$), as used in ECMWF's 4D-Var assimilation of radar precipitation data. Results confirm that for a given rain rate, the RE of a single observation increases with the size of the target grid box and the occurrence of convective precipitation (i.e. during mid-latitude summer and in the tropics), and decreases with the accumulation period. The contribution to RE from the small scales turns out to be usually lower than that from the large-scales, but is not negligible. The relative total RE exceeds 100% for weak precipitation, but can drop down to 20% or less for heavier precipitation. This drop in relative RE is even more pronounced for $\ln(RR + 1)$ than for RR , while the range of RE values is expectedly much reduced in terms of $\ln(RR + 1)$.

Since limited availability of real-time information on rain gauge spatial variability is anticipated, this study proposes a simple parametrisation of RE in terms of $\ln(RR + 1)$ that only depends on target resolution and day of the year, with a distinction between mid-latitudes and tropical regions. A month-dependent parametrisation of precipitation spatial correlations as a function of separation distance has also been formulated. Finally, the reduction of RE due to spatial correlations of the rain field and to the availability of multiple nearby rain gauges is considered. These parametrisations are expected to be applicable to mid-latitude and tropical rainfall over flat terrain and to 6-hour rain accumulations only.

1 Introduction

Rain gauge (RG hereafter) observations have been used for more than a century to improve our knowledge of the spatial and temporal distribution of precipitation over land areas worldwide. Mainly three different types of RG are employed: (1) non-recording gauges (a simple bucket), (2) weighing instruments (time evolution of the bucket weight) and (3) tipping-bucket (TB hereafter) gauges, which electronically counts the number of tips of a small (0.2-0.5 mm) seesaw-like container, as precipitation fills it.

Even though the measurement principle is quite simple, actual RG observations may be affected by a large variety of errors.

First, systematic instrumental errors (WMO 2008) can occur as a result of

- wind-induced undercatch due to aerodynamic effects around the RG (increases with collector height above ground, wind velocity and in the presence of light rain or snow),
- mis-calibration of TBs,
- loss through the wetting of the inner walls (all RGs) and during emptying of the container (especially for non-recording RGs),
- splashing away from the collector,

- evaporation between consecutive measurements (especially for 6-hourly synoptic station observations with non-recording RGs).

The error associated to wind is usually the largest (typically 2 to 10% for rain, up to 10 to 50% for snow).

The second type of errors are "local" random errors, which mainly include

- discrete time sampling errors of TBs,
- variations of the wind effect caused by turbulent airflow around the RG,
- clogging of the collector (e.g., due to leaves or insects),
- failure of a TB to tip (mechanical or electrical problem).

Experimental studies using several RG over areas well below 100 metres in size (e.g., Ciach 2003, Subedi and Fullen 2009) suggested that local random errors for accumulations longer than 1 hour should remain below 5%, except in very light rain rate or in snow. Besides, "local" random errors usually decrease with accumulation length.

The third type of errors, which arise when RGs are used to infer precipitation information well beyond their immediate vicinity, are referred to as representativity errors (RE hereafter). For instance, RE can become significant when RGs are to be compared with precipitation fields produced by numerical weather prediction (NWP) models, since the latter are usually assumed to be spatial averages on the model horizontal grid (from 100 m in cloud resolving models to 300 km in climate models). The discrepancy between individual RG point measurements and corresponding grid-box averaged observed precipitation values is expected to grow when the grid becomes coarser, but also over steep orography or in convective precipitation events (due to increased small-scale variability). At the same time, RE is likely to increase when time accumulation length gets shorter. In terms of magnitude, RE is expected to be the dominant source of observational errors for most applications involving the comparison of RG data to equivalent NWP model fields. This is true in model validation exercises, but also in the context of data assimilation, which is the primary goal of this work.

The aim of data assimilation is to blend information coming from a set of observations with a priori information originating from an NWP model in order to produce optimal three-dimensional representations of the atmospheric state (called the analyses). These analyses can then be used to initialize NWP forecasts. Over the last decade, various data assimilation approaches have been implemented by several operational weather centres (e.g., USA, Japan, UK, France) to assimilate instantaneous ground-based radar observations from their national networks, with some degree of success. These methods include latent heat nudging (Macpherson 2001), diabatic initialization (Ducrocq *et al.* 2002) and variational data assimilation, such as 3D-Var (Caumont *et al.* 2010) or 4D-Var (Lopez and Bauer 2007 ; Lopez 2011; Sun 2005; Koizumi *et al.* 2005). Besides, it has recently become possible to assimilate ground-based radar precipitation estimates that are accumulated over several hours (Lopez 2011), which was shown to improve the validity of the fundamental linearity assumption in 4D-Var.

However, as far as RGs are concerned, the lack of information about RE estimates has hindered the progress towards their use in operational global data assimilation systems. Indeed, the assimilation process requires the specification of reasonably accurate error statistics for each observation, which should include RE. Therefore, the aim of the present study is to quantify RE for point measurements of precipitation at spatial scales ranging from 15 to 80 km and for time accumulations between 15 minutes and 6 hours. This is achieved by estimating the spatial variability of precipitation from both ground-based weather radar data and high-density RG observations, over different regions of the globe. In addition, an estimation of the reduction of RE due to precipitation spatial correlations and to the availability of

multiple nearby RGs is proposed.

It should be emphasised that RE estimates obtained in this study will only be valid for relatively flat terrain regions, since orography often degrades the quality and representativity of both RG and radar observations (e.g., Šalek *et al.* 2004). Their applicability to polar regions will also be questionable due to the unavailability of relevant precipitation datasets at high latitudes.

Section 2 introduces the methodology employed here to obtain RG RE estimates, while section 3 offers a brief description of each observational dataset used in this work. Statistical results are presented in section 4. A discussion is given in section 5 on how these statistics have been utilised to establish a simple definition of RE that might be included in the future assimilation of RG observations in 4D-Var. Section 6 summarises the findings from this study and their potential applications.

2 Methodology

2.1 Estimation of representativity error

The main assumption in the present work is that reasonable estimates of RG RE can be obtained for selected target horizontal resolutions (15, 40 and 80 km here) by computing the spatial variability of precipitation measurements inside horizontal boxes with matching area.

More generally, if n rain observations (RR_i , with $i = 1, \dots, n$) are available inside a certain domain with size A , RE can be approximated by the rainfall spatial standard deviation

$$\sigma = \sqrt{\frac{1}{n-1} \sum_{i=1}^n [f(RR_i) - f(\overline{RR})]^2} \quad (1)$$

where \overline{RR} denotes the mean of all rain observations over the domain. Therefore it is assumed that RE and σ mean the same thing and both terms will be used indiscriminately hereafter. Function f in Eq.(1) is a variable transform that may be applied to the precipitation field, for instance for the purpose of making the distribution of background errors closer to normality in the context of data assimilation. Here, statistics will be computed both for the precipitation rate itself (RR in mm h^{-1}) and for the quantity $\ln(RR[\text{mm h}^{-1}] + 1)$ (LRR hereafter). This logarithmic transform was initially proposed by Mahfouf *et al.* (2007) and subsequently implemented by Lopez (2011) to assimilate ground-based radar data in ECMWF's 4D-Var system. Since it is likely to be used also in future attempts to assimilate RG observations, it is essential to obtain RE estimates for this particular variable as well.

Since no high-density precipitation observations are available on the global scale, the strategy proposed here is to assess rain spatial variability from ground-based radar precipitation estimates, on the one hand, and from high-density RG networks, on the other hand. Radar data should help to assess the contribution to RE from scales larger than a few kilometres, which is denoted σ_L . On the other hand, RG measurements are expected to provide a rough estimate of the contributions from all scales below the size of the RG network, in particular from sub-kilometre scales. Given that most high-density RG networks used in this study do not cover an area larger than 16 km^2 , the main contribution to RE estimates based on RGs will come from scales smaller than a few kilometres and will be denoted σ_S .

It can be shown that total RE (in other words σ) can be approximated by summing up the two variances that are computed for the large and the small scales (i.e. from radars and small-size high-density RG

networks, respectively), that is

$$\sigma \approx \sqrt{\sigma_L^2 + \sigma_S^2} \tag{2}$$

It should be noticed that RGs can allow the direct estimation of total RE only when the size of the RG network exceeds the target resolution, which is the case here only with the South Korean RG dataset (see section 3.4).

2.2 Display of statistics

For each dataset used here, the scatter plot of σ versus $f(\overline{RR})$ is plotted and a fitting curve is constructed based on a locally weighted scatterplot smoothing (LOESS) method (Cleveland 1979). In this fitting procedure, a least-square-weighted local polynomial fit is obtained, in which a higher weight is assigned to nearby points than to remote ones. The fitting algorithm employed in the present work is identical to the one applied by Wood *et al.* (2000) to their rain gauge observations.

A Monte-Carlo bootstrapping method (Efron and Tibshirani 1986) similar to that employed by Wood *et al.* (2000) is used to assess the uncertainty of the LOESS fitted curve. In this approach, the original dataset of length L is split into blocks of length $L_b \ll L$ and a random re-sampling with replacement of certain blocks is performed in order to construct several hundreds of new datasets of length L , for each of which a LOESS fitted curve can be calculated. The spread of the distribution of these fitted curves yields an estimate of the uncertainty. Practically here, vertical bars show the spread between the 5th and 95th percentiles of the statistical distribution of all y-values of the LOESS fitted curves.

An example of scatter plot of σ versus \overline{RR} , with superimposed LOESS fitted curve (for the original non-resampled dataset) and associated uncertainty bars, is displayed in Fig. 1. In the following, the cloud of individual points will be omitted so as to improve plot legibility and to permit the superimposition of various datasets.

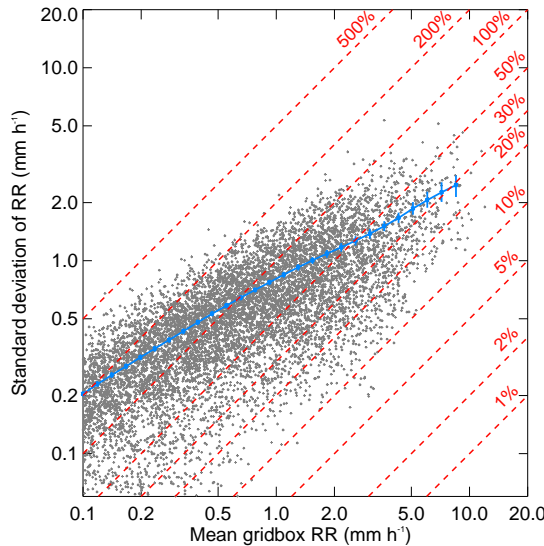


Figure 1: Example of scatter plot (grey crosses) of σ (y-axis) versus \overline{RR} (x-axis) with LOESS fitted curve (blue line) and associated uncertainty bars (vertical blue bars). Red dotted isolines of the ratio σ / \overline{RR} in % are also drawn.

3 Description of datasets

3.1 NCEP Stage IV precipitation data

NCEP (National Centers for Environmental Prediction) Stage IV hourly precipitation data combine precipitation estimates from about 150 Doppler NEXt-generation RADars (NEXRAD) with about 5500 rain gauge measurements over the conterminous USA (Baldwin and Mitchell 1996; Lin and Mitchell 2005). During the production process, data from the original radar pixels (the size of which increases with radar range) are averaged onto a 4-km resolution polar-stereographic grid.

Technically speaking, NEXRAD corresponds to the so-called WSR-88D (Weather Surveillance Radar, 1988, Doppler) (Fulton *et al.* 1998). Each NCEP Stage IV precipitation analysis is initiated 35 min after the end of each hourly collection period and may be updated over a period of several hours with new data coming from the twelve USA regional centres. A first inflow of automatically generated precipitation data is available within a few hours after the accumulation time, while a second inflow of updated manually-quality-controlled data becomes available later (with a delay of up to 12 hours). The spatial coverage of the early release is usually not far away from its maximum extent. In this work, manually quality controlled data were obtained from the JOSS/UCAR (Joint Office for Science Support/University Corporation for Atmospheric Research) archive (website: <http://www.joss.ucar.edu/codiac/>). In the following, these observations will be referred to as "NEXRAD" observations for simplicity.

These data are representative of a broad range of mid-latitude and tropical weather regimes, depending on season and latitude. It should also be noted that only data located east of 105°W have been used in order to avoid the possible degradation in the quality of ground-based radar rainfall estimates over the Rocky Mountains (due to radar beam blockage or orographic enhancement of precipitation). Besides, given the large amount of data to be processed, the data sample has been limited to one year for RE computations (see Table 1). Note however that three years (December 2006–November 2009) of NEXRAD data have been used for the calculations of spatial correlations presented in section 5.3.

3.2 OPERA rain composites

The OPERA (Operational Programme for the Exchange of weather RADar information) Pilot Data Hub (Holleman 2008) is based at the Met Office in Exeter (UK) and provides 15-min precipitation rates obtained from about 150 operational ground-based weather radars over Europe. Typically, these 15-min data are averages over three successive radar scans. OPERA European composites are produced in quasi-real time (within 30 minutes) by combining the data received from each individual countries, following the method described in Harrison *et al.* (2006). It should be noted that countries may send either single radar data or already processed national composites to the OPERA Pilot Hub, which might result in inhomogeneities in the final European composites. At the level of the Data Hub, quality control procedures are applied to single site data to identify and remove ground clutter, anomalous propagation and occultation occurrences, as well as to correct for vertical profile effects associated to bright band occurrence, resolution degradation with range and orographic enhancement of precipitation. On the other hand, no particular quality control is performed on the national composites other than the one performed by the national services themselves. The final OPERA composites are provided in BUFR format and on a Lambert's azimuthal equal area projection (tangent point 55°N and 10°E), with a pixel size of 4 km.

In this study, OPERA data have been restricted to 5°W–15°W and 48°N–53°N (Germany) so as to be representative of relatively flat terrain and mid-latitude meteorological conditions. Another justification

for this choice lies in the fact that, according to Lopez (2008), OPERA data exhibit their best quality over Germany. Similar to NEXRAD, the period of the OPERA data used here extends from 1 December 2008 to 30 November 2009.

3.3 Darwin radar data

Rainfall estimates obtained from the ground-based scanning C-band polarimetric precipitation radar located near Darwin in Australia (location: 131°03'E/12°15'S; Keenan *et al.* 1998) were provided by Monash University, Melbourne, for three consecutive rainy seasons (November to April) from 2004 to 2007. The spatial and temporal resolutions of the CAPPI (Constant Altitude Plan Position Indicator) precipitation data are 2.5 km and 10 mn, respectively. This dataset is representative of monsoon-type tropical weather regimes, often characterised by intense convective activity and heavy rainfall.

3.4 South Korea rain gauge data

South Korea benefits from a rather high-density network of about 520 TB RGs (Sohn *et al.* 2010), which corresponds to an average separation distance just below 15 km. Data were obtained in the form of hourly accumulations for each rain gauge and for the year 2009. These data are expected to be representative of a wide range of weather regimes, from cold mid-latitude conditions in winter to subtropical conditions during summer.

3.5 HYREX data

The Hydrological Radar Experiment (HYREX) was conducted in Somerset in the UK to study the spatial and temporal variability of precipitation over the River Brue catchment area, mainly for hydrological purposes (Moore *et al.* 2000). A network of 49 TB RGs was installed over the entire catchment area, with two high-density 4-km² boxes featuring 8 gauges each. Also available from the HYREX database were data from the two ground-based C-band precipitation radars located at Wardon Hill, Dorset (2°34'W/50°48'N) and Cobbacombe, Devon (3°25'W /50°58'N). In this study, data from the low-relief 4-km² box RGs as well as from the two radars have been used over the period September 1993 to May 2000. These data were supplied by the British Atmospheric Data Centre from the NERC (Natural Environment Research Council) HYREX Dataset (<http://www.badc.rl.ac.uk/data/hyrex/>).

3.6 Walnut Gulch rain gauges

The 149 km² Walnut Gulch Experimental Watershed is located in southeastern Arizona (USA; location: 110°04'W/31°43'N) and is currently equipped with 88 operational weighing-recording RGs. A more detailed description of the instrumentation can be found in Goodrich *et al.* (2008) and data are available from the USDA-ARS (United States Department of Agriculture/Agricultural Research Service) website on <http://www.tucson.ars.ag.gov/dap/digital/event.asp>. This site is characterised by a subtropical semi-arid climate with dry springs and precipitation peaking around mid-summer (convective). Measurements used in the present work are those from 12 RGs (namely gauges number 27, 28, 31, 32, 33, 39, 40, 71, 74, 80, 87 and 398) that are located inside a 16 km² box in the northern part of the watershed, from 1 January 1999 to 31 December 2010.

3.7 USDA Riesel rain gauges

The USDA-ARS Grassland Soil and Water Research Laboratory watersheds near Riesel, Texas (USA; location: 96°53'W/31°28'N), provide long-time series (since 1937) of precipitation recordings from up to 57 RGs (see Harmel *et al.* 2003). Data can be accessed on <http://www.ars.usda.gov/Research/docs.htm?docid=10216>. The Riesel region is characterised by flat terrain and a subtropical subhumid climate, with frontal precipitation in winter and heavy convective rainfall during the warmer season, peaking in May. To ensure temporal continuity and spatial proximity, only 13 TB RGs (namely gauges number w1b, w5a, w2a, w6, w4, w3, w2, 84a, 75a, 70a, 89, 70, 69), which are located inside a 4-km² area, have been selected here, over the period 1 January 1970 to 31 December 2010.

Dataset	Resol./RG density	Location/Domain	Temporal coverage	Instrument Type
NEXRAD	4 km	Eastern half USA	Dec 2008-Nov 2009	C-band Dop. Rad.
OPERA	4 km	Europe (Germany)	Dec 2008-Nov 2009	C-/S-band Dop. Rad.
Darwin	2.5 km	Darwin, Australia	Dec 2008-Nov 2009	C-band Pol. Rad.
HYREX Rad.	2 km 2 km	Wardon Hill, UK Cobacombe, UK	Sep 1993-Apr 2000 Feb 1994-Apr 2000	C-band radar C-band Dop. Rad.
South Korea	520 RGs/10 ⁵ km ²	South Korea	Year 2009	TB RG
HYREX RGs	8 RGs/4 km ²	Somerset, UK	Sep 1993-May 2000	TB RG
Walnut Gulch	12 RGs/16 km ²	Arizona, USA	Jan 1999-Dec 2010	WR RG
USDA Riesel	13 RGs/4 km ²	Texas, USA	Jan 1970-Dec 2010	TB RG

Table 1: Main characteristics of precipitation observational datasets used to assess RE: spatial resolution or RG density, geographical location, sample length and instrument type. Abbreviations: Dop.=Doppler, Pol.=polarimetric, Rad.=radar, TB=Tipping-Bucket, WR=Weighting-Recording.

4 Results

Results from each available dataset will be presented in the form of fitted curves of the standard deviation of precipitation observations, σ , plotted against the mean precipitation value, $f(\overline{RR})$, as detailed in section 2.2. Statistics have been computed for three different target grid box sizes (15, 40 and 80-km) and for each season of the year as well as for the whole year. Furthermore, three precipitation accumulation lengths have been considered: 6 hours (for all datasets), 1 hour and 15 mn (for a few datasets). Only a selected subset of these statistics will be shown here with a particular focus on the 6-hour accumulation length. Indeed, the latter is representative of most synoptic station RG measurements and was found to be the optimal accumulation length for the assimilation of precipitation observations in 4D-Var (Lopez 2011). Lastly, statistics for both RR and LRR will be shown on panels (a) and (b) of each figure of this section, respectively.

4.1 Ground-based radars

Statistics obtained from these datasets provide an estimate of precipitation RE resulting from scales ranging from a few kilometres to the size of the selected target grid box (15, 40 or 80-km). In other words, this estimate of RE corresponds to σ_L in Eq.(2).

Figure 2 displays σ_L against $f(\overline{RR})$ for 6-hourly precipitation accumulations, for all radar datasets and for 15-km target grid boxes. This corresponds to the highest spectral truncation (T1279) currently used in ECMWF's Integrated Forecasting System (IFS). In this figure, statistics apply to the entire period of each dataset (see Table 1).

Both panels show that σ_L monotonically increases with $f(\overline{RR})$ for most datasets. Only NEXRAD and Darwin exhibit a curve which slightly drops for values of $\ln(\overline{RR} + 1)$ larger than 1.0 (Fig. 2.b). As expected from the application of a logarithmic transform, the range of σ_L values is higher for RR (0.08-7.0 mm h⁻¹) than for LRR (0.07-0.4). It is also remarkable that the spread among all radar datasets is not too wide, with the exception of Darwin data for which σ_L is systematically larger, especially for lower precipitation rates. This can be explained by the predominance of convection at the tropical site of Darwin, which is accompanied by strong horizontal variability of the precipitation field.

In relative terms, the ratio $\sigma_L/f(\overline{RR})$ usually decreases with $f(\overline{RR})$ from around 100% to 20% for RR and from about 70% to 10% for LRR . For Darwin data, the ratio exceeds 100% for the smaller precipitation amounts.

It is also worth noting that the smaller sample size of the Wardon Hill and Cobbacombe radar datasets results in increased uncertainty (i.e. wider error bars, see section 2.2). As an illustration of seasonal variability, Fig. 3 displays σ_L against $f(\overline{RR})$ for 6-hourly NEXRAD precipitation on a 15-km horizontal scale and for each season and the whole year. It is clear that RE is weakest in winter and highest in summer, as a result of the predominance of stratiform versus convective precipitation systems, respectively, except for higher precipitation rates (mostly convective). On the other hand, spring and autumn exhibit σ_L values close to yearly statistics. As an example of the dependence on target horizontal resolution, Fig. 4 shows NEXRAD statistical results computed at 15, 40 and 80-km resolutions and for the whole year. For any given $f(\overline{RR})$ value, RE roughly doubles when the size of target boxes is increased from 15 to 80 km. This simply reflects the corresponding reduction in the amount of information that any single 4-km radar observation can provide about the target-box mean precipitation.

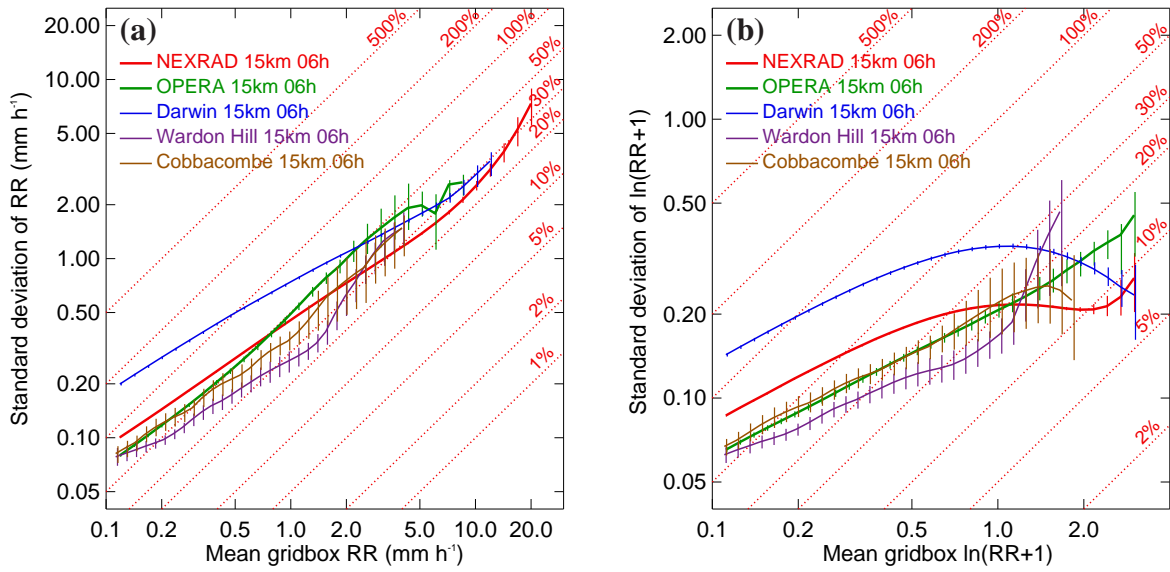


Figure 2: Standard deviation of 6-hourly accumulated precipitation as a function of mean precipitation value computed over 15-km boxes and for all radar datasets used in this study: NEXRAD and OPERA networks, Darwin, Warden Hill and Cobbacombe individual radar sites. Panels (a) and (b) show statistics in terms of RR and LRR, respectively. Statistics are valid for the periods mentioned in Table 1. Red dotted isolines indicate standard deviation normalised by mean gridbox precipitation (in %). Vertical bars show the uncertainty of each curve, as assessed from the bootstrapping method described in section 2.2.

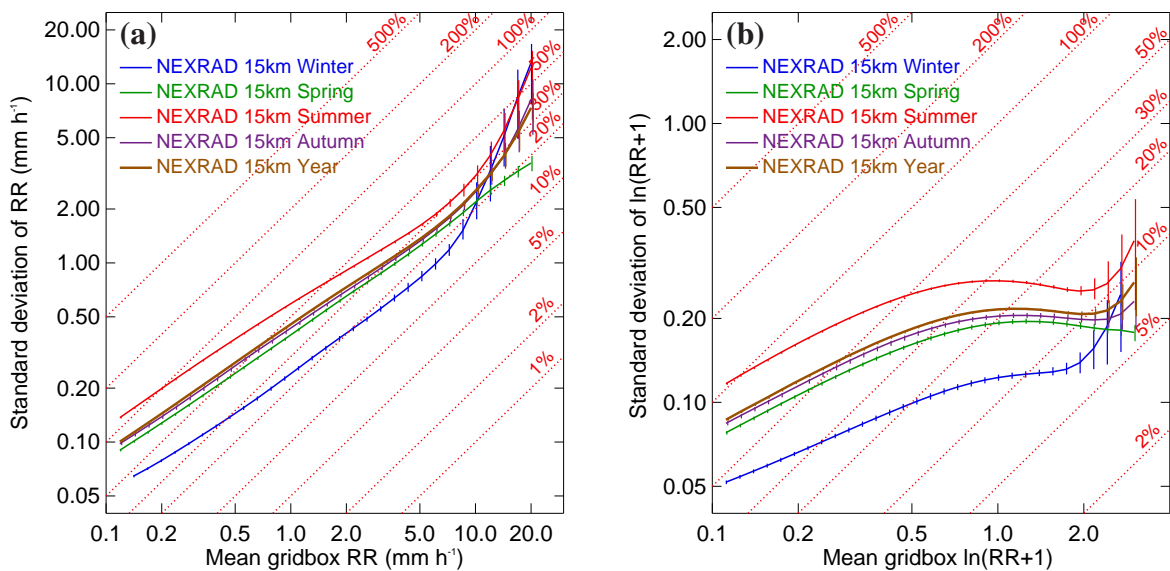


Figure 3: Same as in Fig. 2, but for NEXRAD data only and for various seasons.

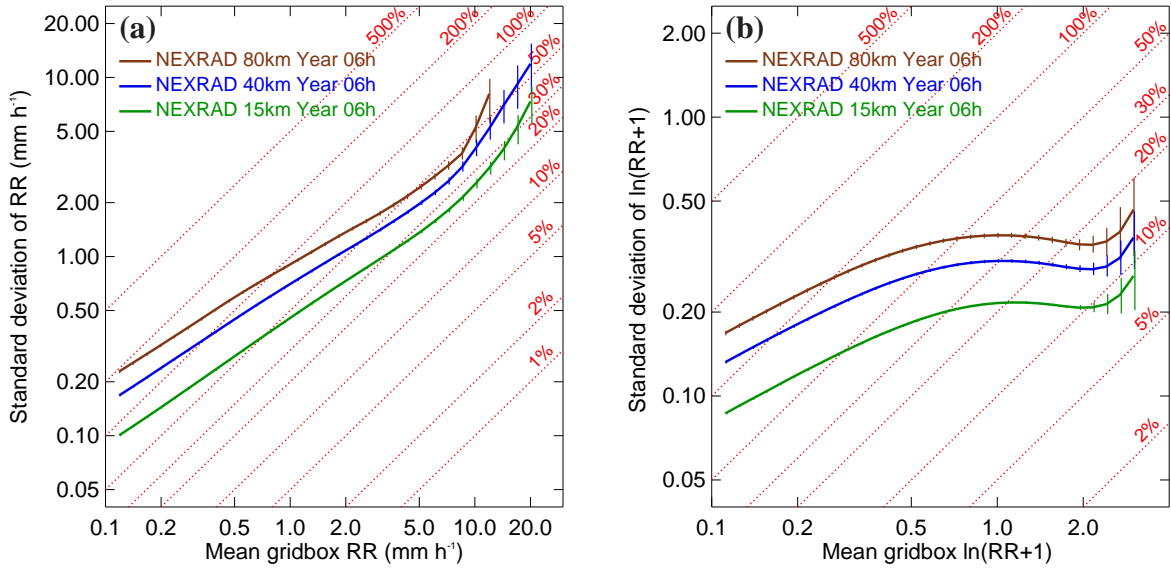


Figure 4: Same as in Fig. 2, but for NEXRAD data only and for target horizontal resolutions of 15, 40 and 80 km.

4.2 High-density rain gauge networks

Statistics obtained from these datasets give an estimate of precipitation RE on scales finer than a few kilometres, to complement those obtained from radars. This estimate of RE therefore corresponds to σ_5 in Eq.(2).

Figure 5 displays σ_5 against $f(\overline{RR})$ for 6-hourly precipitation accumulations, computed from all high-density RG datasets and over the respective network areas given in Table 1. Statistics are valid for the entire length of each dataset. The curves show a similar slope to those obtained for radars in Fig. 2, but the differences among RG networks is larger. Walnut Gulch and USDA Riesel networks, both based in southern USA, exhibit σ_5 values that are between three and four times as large as those for the UK-based HYREX network, which can be attributed to more frequent convection over Arizona and Texas. The HYREX RG $\sigma_5/f(\overline{RR})$ ratio is in fact remarkably low, ranging from 40% for low rain rates to 13% (resp. 7%) for high rain rates in RR (resp. LRR) space. This is the result of the predominance of stratiform precipitation in North Atlantic cloud systems, throughout the year. Figure 6 quantifies the expected increase of σ_5 (by a factor between 3 and 5) when precipitation accumulation length is shortened from 6 hours to 15 mn, in the case of the HYREX RGs. One should also note that the increase of σ_5 when going from 1 hour to 15 mn is as large as that obtained when going from 6 hour to 1 hour accumulations. Besides, this degradation of σ_5 seems to be stronger for low rain rates, which might be related to the occurrence of isolated showers at scales below 2 km.

4.3 South Korean rain gauge network

Statistics calculated from this dataset should be representative of all scales up to the the target horizontal resolution, including scales finer than the distance between rain gauges. The resulting estimate of RE therefore corresponds to σ in Eq.(2).

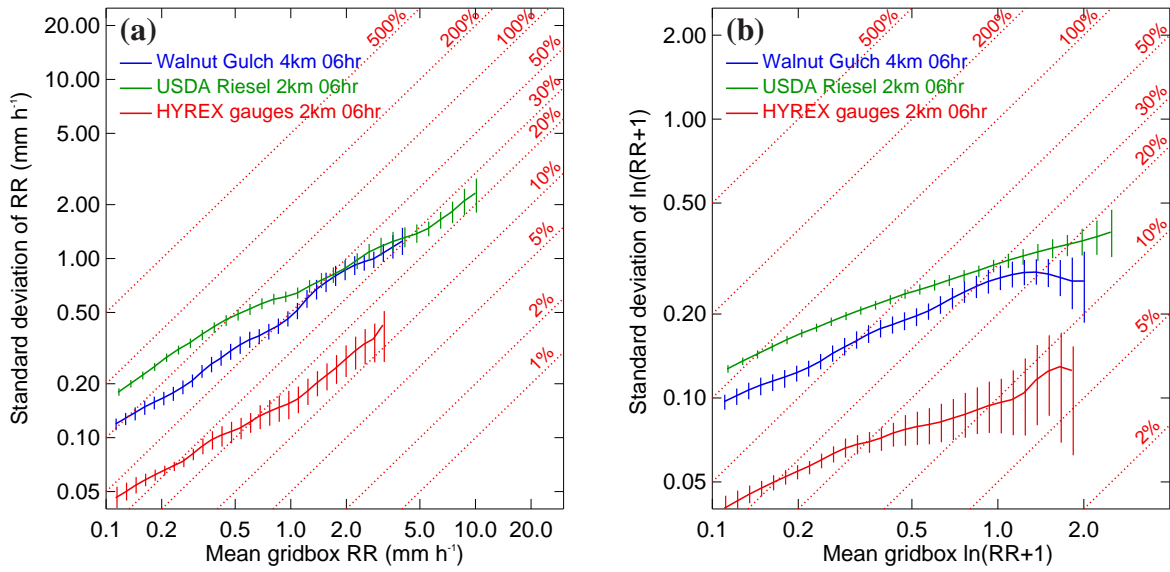


Figure 5: Standard deviation of 6-hourly accumulated precipitation as a function of mean precipitation value from all high-density rain gauge datasets used in this study: Walnut Gulch, USDA Riesel and HYREX networks. Same layout as in Fig. 2.

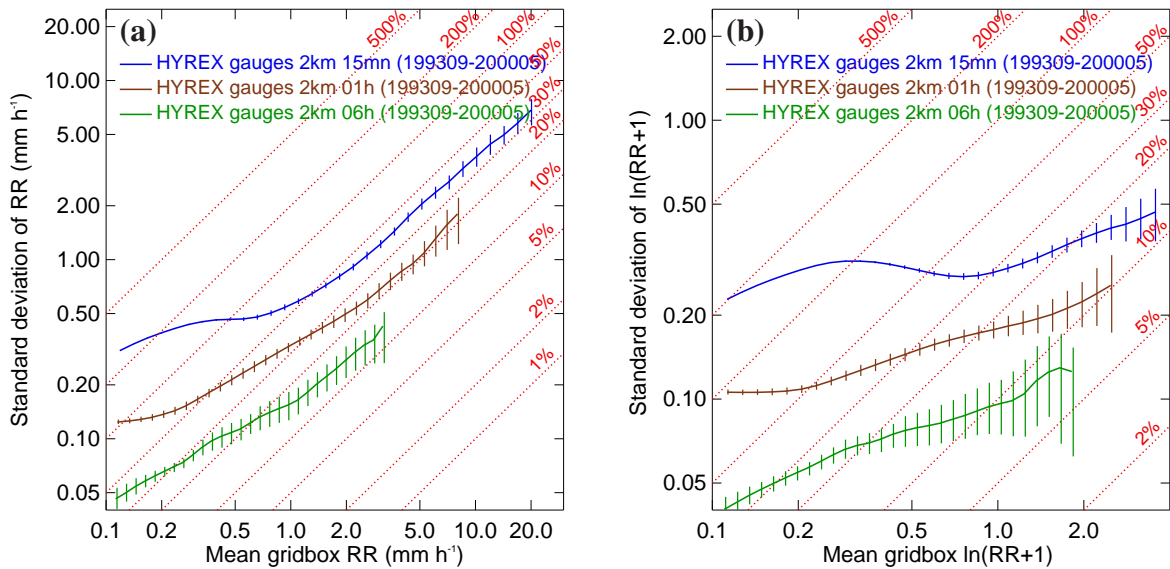


Figure 6: Standard deviation of precipitation as a function of mean precipitation value from the HYREX high-density rain gauge network and for rain accumulation lengths of 15 mn, 1 hour and 6 hours. Same layout as in Fig. 2.

Figure 7 shows RE as a function of $f(\overline{RR})$ for South Korean RGs, for three seasons (cold, transition and warm) and for two target horizontal resolutions (0.4 and 0.8 degree, i.e. ≈ 40 and 80 km). Statistics at 0.15 degree resolution turned out to be impossible to calculate due to the lack of points in each target box, as the mean separation distance over the South Korean RG network is about 15 km. "Cold" and "warm" seasons refer to the periods December-March and June-September, respectively, while the "transition" season comprises the months of April, May, October and November.

Consistent with what was found from NEXRAD data (see Fig. 3), RE is clearly higher during the warm season (convective activity) than during the cold season (stratiform precipitation), with the transition season lying in-between. Also consistent with Fig. 4, RE increases when target horizontal resolution is changed from 0.4 to 0.8 degree. Quantitatively, σ values from South Korean RG observations are comparable to those displayed in Fig. 4 from NEXRAD data. Indeed, yearly values of σ for RR (panel (a)) range from 0.2 for the lowest rain rates to 3.0 mm h^{-1} for rain rates of 10 mm h^{-1} . In terms of LRR (panel (b)), σ varies between 0.15 and 0.4 when LRR ranges from 0.1 to 2.0. However, the seasonal spread of σ for South Korean RGs (Fig. 7) is slightly narrower than for NEXRAD data (not shown), especially for rain rates lower than 1 mm h^{-1} .

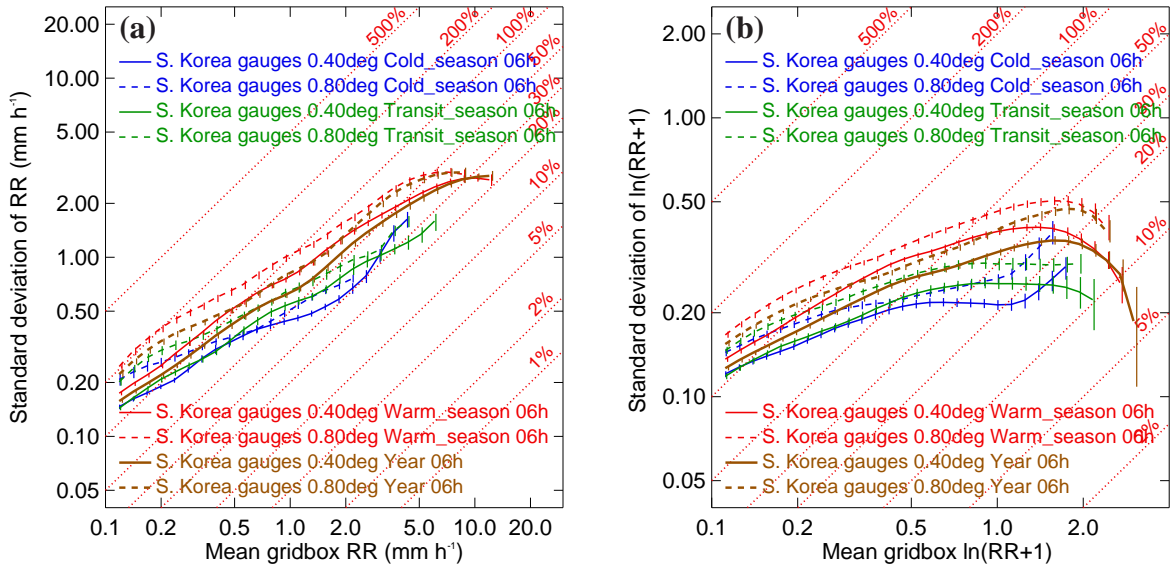


Figure 7: Standard deviation of 6-hourly accumulated precipitation as a function of mean precipitation value from the South Korean rain gauge network. Statistics are displayed for the cold, transition and warm seasons and for two target horizontal resolutions of 0.4 and 0.8 degree, as indicated in the legend. Same layout as in Fig. 2.

5 Discussion

5.1 Parametrisation of single rain gauge representativity error

Results presented in section 4 using all precipitation datasets helped to identify and quantify the monotonic increase of σ and the monotonic decrease of $\sigma/f(\overline{RR})$ with $f(\overline{RR})$. Therefore, an ideal formulation

of RE for precipitation point-measurements ought to be obtained through a function describing the σ - $f(\overline{RR})$ relationship, with some additional dependence on season or precipitation type (convective versus stratiform), and maybe on geographical location and orography (rugged versus flat terrain) as well.

However, the development of such formulation for NWP applications suffers from several practical limitations. First, the actual value of \overline{RR} , which would typically be observed precipitation averaged over a model grid box in this case, is usually unknown. The only information available originates from individual RG observations, which are usually sparsely distributed in space. This makes it impossible to compute RG RE using a σ - $f(\overline{RR})$ relationship.

Secondly, the inclusion of a direct dependence of RE on precipitation type could only be based on additional information coming either from other instrumental platforms (e.g., satellites) or from the forecast model. However, other types of observations that are colocated with RGs and capable of providing reliable information about precipitation type are seldom available on the global scale and in real-time (operational context). The alternative of using model fields (e.g., convective available potential energy) to identify precipitation type would be problematic as well, if only because of potential misplacements or mis-timing of convective/stratiform events in the model, even at short forecast ranges. Furthermore, since conventional RG measurements are provided in the form of rainfall accumulations over at least 6 hours, a change in precipitation type is likely to occur over such a period of time as a result of the displacement of cloud systems.

Therefore the only possible solution for applications in NWP and in data assimilation is to specify a value of RE which is (unfortunately) independent of precipitation amount, but which can still be modulated according to season. This seasonal dependence would crudely account for typical changes in precipitation regimes/types throughout the year. It should be emphasised that the lack of dependence of RE on rain amount should be less of an issue for LRR than for RR , since the range of σ variations is much smaller for the former variable than for the latter. This can be seen by comparing panels (a) and (b) in all plots of section 4. One should also note that LRR is the variable used to assimilate precipitation observations at ECMWF (Lopez 2011).

To ease the definition of "universal" seasonal-dependent values of LRR RE, Figure 8 offers a visual representation of the range of σ values derived from all datasets for different seasons and for target resolutions of 15, 40 and 80 km. For any individual curve of the type shown in section 4, the range is defined by the lowest and highest LRR RE values for which the uncertainty is not too large (namely $y_{top} \leq 2 y_{bottom}$ for the error bar). From Fig. 8 and with the help of the plots presented in section 4 and by taking into account Eq.(2), the following (rather crude and subjective) formulation for RE has been established:

$$\sigma(D) = \sigma_0 + \Delta\sigma \sin \left\{ \frac{\pi}{2} \left(\frac{D-112}{91} \right) + \delta_{hemis}\pi \right\} \quad (3)$$

where D is the day of the year and δ_{hemis} is equal to 0 for the northern hemisphere and 1 for the southern hemisphere. Parameters σ_0 and $\Delta\sigma$ depend on target resolution and geographical location according to Table 2. In this table, tropics are assumed to extend between 25°S and 25°N and mid-latitudes between 25° and 60° in both hemispheres. Figure 9 illustrates the variations of σ given by Eq.(3) for the three selected target resolutions and for both northern mid-latitudes and tropics (constant value). The main assumption is that RE is constant throughout the year in the tropics to account for the omnipresence of convective precipitation, while in the mid-latitudes RE fluctuates with season, with lower values in winter (stratiform rain) and higher values in summer (convective rain).

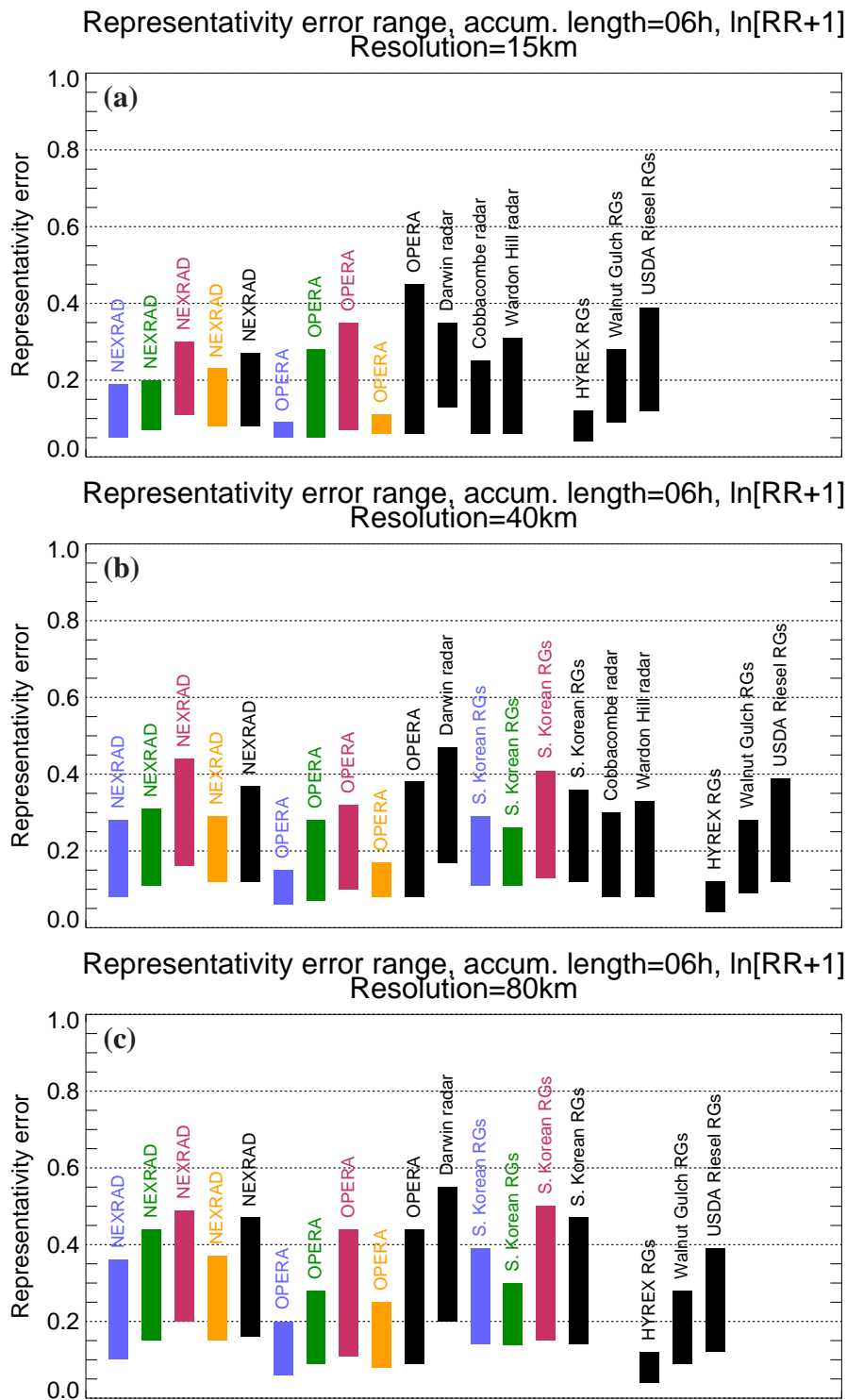


Figure 8: Range of representativity error in terms of LRR from all datasets and for target resolutions of (a) 15 km, (b) 40 km and (c) 80 km, as determined from the curves obtained in section 4. Results are for 6-hourly precipitation accumulations. Each vertical bar is labelled with the dataset name and its colour indicates the period of the year: winter (blue), spring (green), summer (red), autumn (orange) and whole year (black). For South Korean RGs, the green bar corresponds to the "transition" season (April, May, October and November). The three high-density RG networks are shown separately on the extreme right of each panel (independent of target resolution).

Target resolution	Mid-latitudes		Tropics	
	σ_0	$\Delta\sigma$	σ_0	$\Delta\sigma$
15 km	0.220	0.070	0.290	0
40 km	0.285	0.085	0.370	0
80 km	0.350	0.100	0.450	0

Table 2: Values of the two parameters σ_0 and $\Delta\sigma$ used in the parametrisation of RE for 6-hourly precipitation accumulations in terms of LRR (see Eq.(3)), for various target resolutions and for mid-latitudes and tropics.

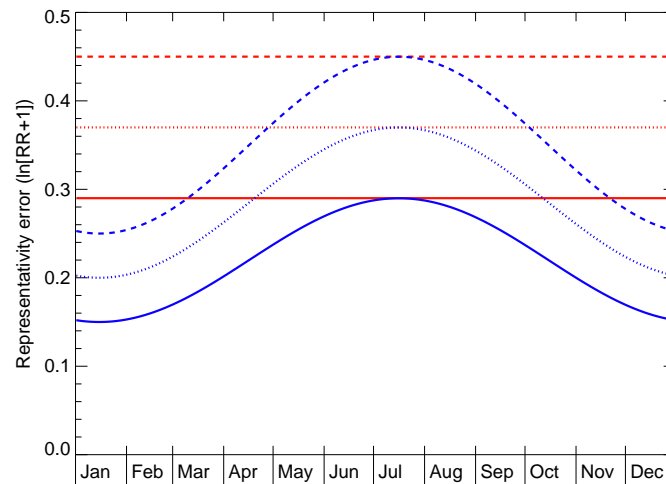


Figure 9: Annual evolution of parametrised representativity error of 6-hourly precipitation accumulations (in LRR space) for target resolutions of 15 km (solid line), 40 km (dotted line) and 80 km (dashed line), according to Eq.(3) and using Table 2. Blue (resp. red) lines are for northern mid-latitudes (resp. tropics).

5.2 Impact of spatial correlations and number of rain gauges on representativity error

As explained earlier, our aim here is to specify RE for the mean value of a set of rain gauges available over a certain target grid box. Even when only one RG is available inside the target grid box, horizontal correlations of the precipitation field are expected to reduce RE compared to the estimate given by Eq.(3). Besides, when several rain gauges are available inside the same target grid box, the increased information content should also lead to a drop in the RE of the RG grid box averaged rainfall.

Morrissey *et al.* (1995) showed that the RE, $\tilde{\sigma}$, for the average of n RGs over the target box can be assessed from the RE of individual point observations, σ , through

$$\tilde{\sigma}^2 = \sigma^2 \left[\underbrace{\frac{1}{n^2} \sum_{i=1}^N \sum_{j=1}^N \rho(\mathbf{d}_{i,j}) \delta(i) \delta(j)}_{T1} - \underbrace{\frac{2}{Nn} \sum_{i=1}^N \sum_{j=1}^N \rho(\mathbf{d}_{i,j}) \delta(i)}_{T2} + \underbrace{\frac{1}{N}}_{T3} + \underbrace{\frac{2}{N^2} \sum_{i=1}^{N-1} \sum_{j=i+1}^N \rho(\mathbf{d}_{i,j})}_{T4} \right] \quad (4)$$

where $\rho(\mathbf{d}_{i,j})$ is the spatial correlation between two rain gauges indexed i and j and separated by the distance $\mathbf{d}_{i,j}$. N is the number of rectangular sub-boxes artificially defined to divide the target area in such way that either 0 or 1 rain gauge is present inside each sub-box, as illustrated in Fig. 10. The

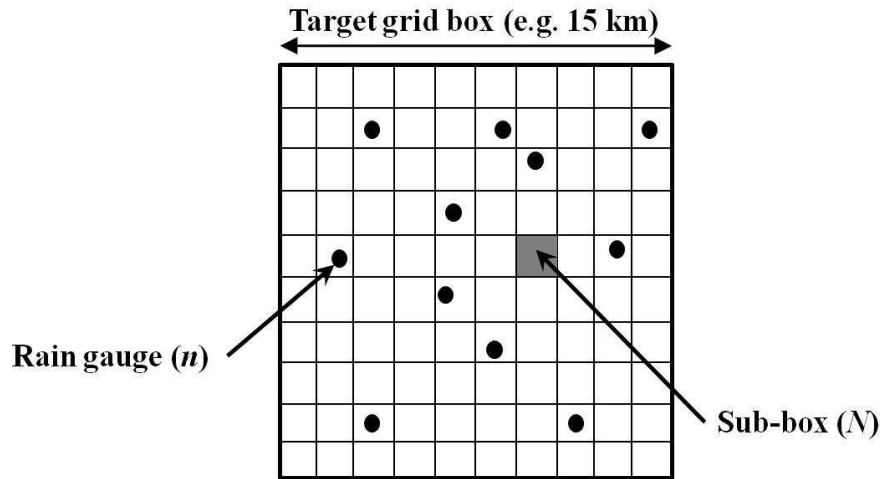


Figure 10: Illustration of the subdividing of a given target box into N sub-boxes for the estimation of the reduction in precipitation representativity error when n rain gauges are available instead of a single one.

main underlying assumption in Eq.(4) is that precipitation over each sub-box is well approximated by the rain gauge measurement it contains, which requires the size of sub-boxes not to exceed a couple of kilometres. It is also assumed that σ is the same for each RG present in the target box. The quantity in large brackets in Eq.(4) is the so-called variance reduction factor. Each term in the brackets correspond to the influence of:

- (T1) the correlations between RGs,
- (T2) the spatial average of correlations around each RG,
- (T3) the definition of sub-boxes (small if N large enough),
- (T4) the spatial average of correlations between sub-boxes.

5.3 Spatial correlations

Spatial correlations between RGs (i.e. $\rho(\mathbf{d}_{i,j})$ in Eq.(4)) should ideally be estimated from high-density RG datasets with good spatial and temporal coverage. However, due to the unavailability of RG datasets that fulfill these requirements, NEXRAD 4-km data have been used instead, since these offer good spatial and temporal coverage. This ensures that the correlation curves are not too noisy. The fact of using 4-km radar data instead of point measurements for this estimation might lead to small differences in spatial correlations (Gebremichael and Krajewski 2004), but these differences are not expected to be significant in data assimilation or model verification applications.

The computation of $\rho(\mathbf{d}_{i,j})$ is based on the method applied in Gebremichael and Krajewski (2004), which uses the bivariate mixed lognormal precipitation distribution of Shimizu (1993).

Resulting 3-year averaged spatial correlations, ρ , as computed from 4-km resolution NEXRAD 6-hourly precipitation accumulations, are plotted for each month in Fig. 11 as a function of separation distance, $\mathbf{d}_{i,j}$, for both *RR* (panel (a)) and *LRR* (panel (b)).

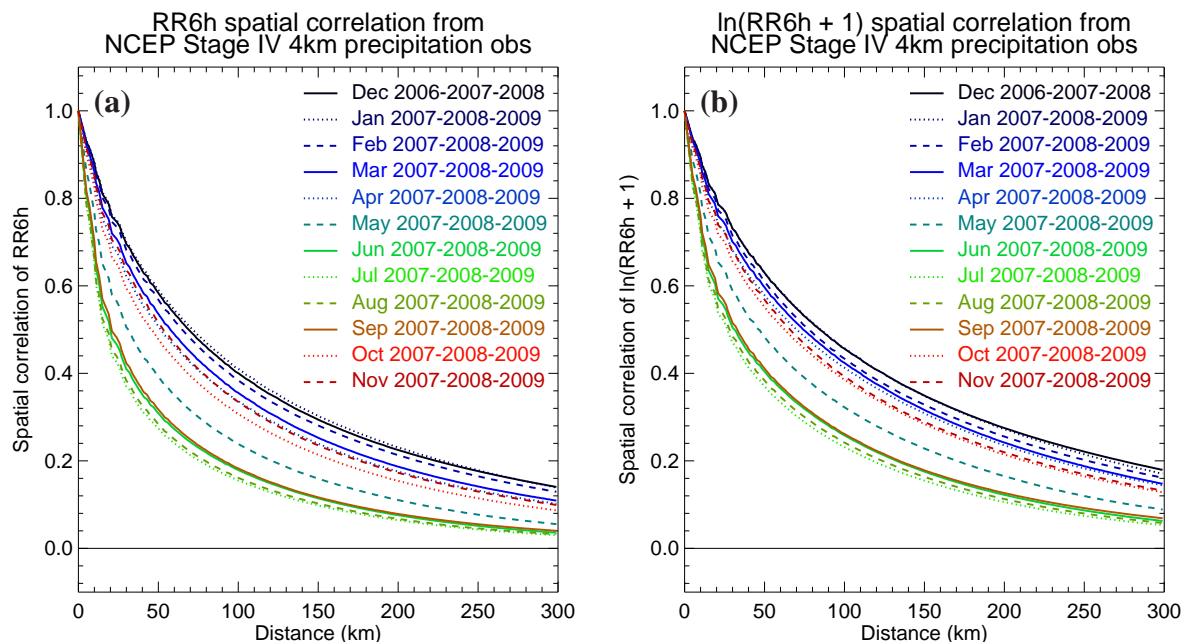


Figure 11: Precipitation spatial correlation as a function of separation distance, as computed from 3 years of NEXRAD 6-hourly precipitation accumulations in terms of (a) *RR* and (b) *LRR*. Each curve corresponds to a given month, as indicated in the legend.

Figure 11 clearly shows that the drop of spatial correlations with separation distance gradually becomes more pronounced when going from winter to summer. The longest span is obtained in January and December, the narrowest in July and August. This is the consequence of the predominance of convective activity during the warmer months, which is characterised by enhanced small-scale variability of precipitation (convective cells embedded in mesoscale systems). In contrast, stratiform precipitation which prevails during winter is usually associated with widespread, rather uniform frontal cloud systems, which explains the broader shape of the spatial correlation curves. April, May, October and November are clearly transition months affected by both types of precipitation. The same seasonal trend of spatial

correlations was found with South Korean RGs, but the curves were somewhat noisier due to the smaller sample size and spatially discrete nature of the data (not shown).

A classical exponential fit to the correlation curves shown in Fig. 11 is proposed as

$$\rho(d) = \exp [b(M) d^{c(M)}] \quad (5)$$

where d is the separation distance (in km) and $b(M)$ and $c(M)$ are coefficients which depend on the month of the year, M . Figure 12 shows the monthly variations of coefficients b and c for both variables RR and LRR in northern hemisphere mid-latitudes. Figure 12 indicate that b and c oscillate rather regularly

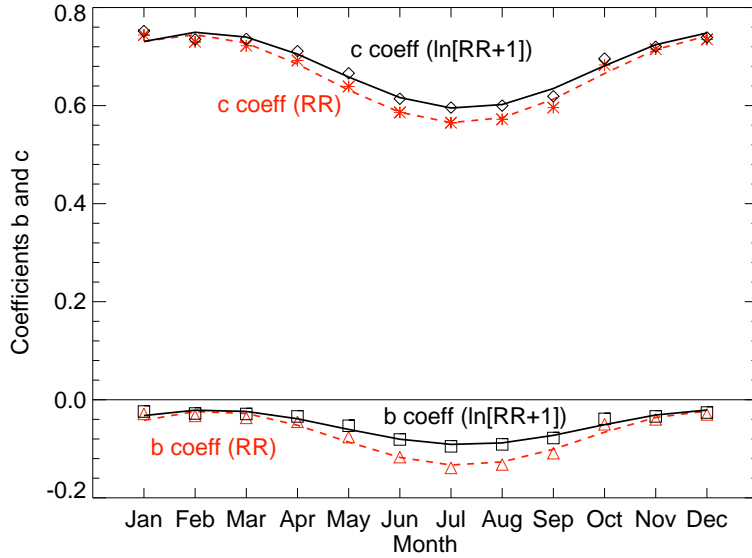


Figure 12: Monthly variations of coefficients b (triangles and squares) and c (diamonds and stars) used in the exponential fit of the spatial correlations of NEXRAD 6-hourly precipitation accumulations, for both RR (red) and LRR (black). The sine curves used to fit monthly values are also shown. This plot is valid for northern mid-latitudes.

between a maximum in January and a minimum in July. Therefore, monthly values of b and c have been fitted with the following sine functions (plotted in Fig. 12)

$$b(M) = b_0 + \Delta b \sin \left\{ \frac{\pi}{2} \left(\frac{M - m_b}{\Delta m_b} \right) + \delta_{hemis} \pi \right\} \quad (6)$$

$$c(M) = c_0 + \Delta c \sin \left\{ \frac{\pi}{2} \left(\frac{M - m_c}{\Delta m_c} \right) + \delta_{hemis} \pi \right\} \quad (7)$$

where b_0 , Δb , m_b , Δm_b and c_0 , Δc , m_c , Δm_c are given in Table 3. This parametrisation is assumed to be applicable in mid-latitude regions.

For the tropics, rough estimates of coefficients b and c have been obtained by restricting the NEXRAD correlation computations to the Peninsula of Florida (south of 29°N). Results (not shown) indicate only weak variations of the two coefficients throughout the year and a drop of correlation with separation distance which is even sharper than for mid-latitude summer months (Fig. 11). This is consistent with the omnipresence of convection all year round and has led to the specification of fixed values of b and c

given in Table 3. The resulting tropical correlation functions are in agreement with those found by Habib and Krajewski (2002) for hourly rain accumulations in the summer over central Florida during the Texas and Florida Underflight Experiment (TEFLUN-B). Here it is assumed that Floridian correlations are representative of the entire tropical band. This may seem rather crude but this is the best we can do, until alternative tropical precipitation datasets with better temporal and spatial coverage become available.

	Mid-latitudes		Tropics	
	<i>RR</i>	<i>LRR</i>	<i>RR</i>	<i>LRR</i>
b_0	-0.078	-0.056	-0.197	-0.164
Δb	-0.055	-0.036	0	0
m_b	4.770	4.803	/	/
Δm_b	2.444	2.481	/	/
c_0	0.655	0.672	0.609	0.623
Δc	-0.090	-0.078	0	0
m_c	4.563	4.711	/	/
Δm_c	2.619	2.548	/	/

Table 3: Values of the eight parameters used to describe the monthly variations of the fitting coefficients b and c for spatial correlations of 6-hourly precipitation accumulations (see Eq.(5), Eq.(6) and Eq.(7)). Values are given for both variables RR and LRR and for both mid-latitudes and tropics. In the tropics, b and c are assumed to be constant throughout the year.

5.4 Practical implementation

Practically, the specification of RE for the average of a set of RGs over a selected model grid box, for instance in the context of data assimilation, would comprise the following steps:

- (1) Determination of the number n and positioning of RGs available inside the model grid box.
- (2) Computation of individual RG RE from Eq.(3) and Table 2.
- (3) Definition of a regular lattice of N sub-boxes containing either 0 or 1 RG each.
- (4) Computation of spatial correlations between sub-boxes using Eqs.(5)-(7) and Table 3.
- (5) Calculation of the final RE of the grid box averaged rain observation from Eq.(4).

Eventually, this RE value would then be added to the other components (see section 1) of the total observation error to be used during the assimilation process.

6 Summary and conclusions

In this work, representativity error has been defined as the error one makes when trying to assess the averaged value of rainfall over a target area (e.g., a model grid box) from a set of point measurements scattered over the same area. In particular, improving our knowledge of RE for RGs is a prerequisite to their possible assimilation in 4D-Var.

A quantitative estimation of RE for individual point measurements has been obtained from various radar and RG datasets over different regions of the globe. Statistics were computed for rain rate but also for

its logarithmic transform ($\ln(RR + 1)$), as the latter variable is already employed in ECMWF's 4D-Var assimilation of ground-based radar precipitation data.

Results confirmed that for a given rain rate, RE increases with the size of the target grid box and occurrence of convective precipitation (i.e. during mid-latitude summer and in the tropics), and decreases with the accumulation period. The contribution to RE from the small scales turns out to be usually lower than that from the large-scales, but is not always negligible, especially in convection. The relative total RE exceeds 100% for weak precipitation, but can drop down to 20% or less for heavier precipitation. This drop in relative RE is even more pronounced for *LRR* than for *RR*, while the range of RE values is expectedly much reduced in terms of *LRR*.

A simple formulation of RE in terms of *LRR* has been established, which includes a dependence on season and target grid box resolution as well as the effect of rainfall spatial correlations. It was not possible to express RE as a function of grid box averaged observed precipitation itself since the latter is usually unknown. It should be emphasised that the coefficients used in the proposed formulation are only valid for 6-hour rain accumulations, which corresponds to the time sampling of most synoptic station RGs, and therefore they should be recomputed if other accumulation lengths are considered.

The proposed formulation of RE involves two main steps. First, an estimate of RE for single point measurements is obtained. Then, the total RE for the set of rainfall observations available over the selected target grid box can be computed, taking into account the influence of precipitation spatial correlations, which tend to reduce RE. In mid-latitudes, single RG RE is assumed to vary sinusoidally according to season from a winter minimum to a summer maximum, as a result of the transition from predominantly stratiform to predominantly convective precipitation regimes. In the tropics, one assumes that single RG RE is constant throughout the year, with values similar to those obtained for mid-latitude summer conditions. One should stress here that the lack of long enough, wide coverage and accurate tropical rainfall datasets clearly hinders our capacity to obtain better statistics over these regions.

The proposed RE parametrisation is mainly intended for data assimilation purposes but could also very well be applied to model validation. In particular, the plan is to employ it as part of the future assimilation of 6-hourly RG observations in ECMWF's 4D-Var system to specify reasonable observation errors at the scale of the model grid box.

Acknowledgements

We would like to thank Alan Geer (ECMWF) for his early review of this paper. NCEP should be acknowledged for producing and JOSS/UCAR for providing the Stage IV precipitation observations used in this study. The British Atmospheric Data Centre should be thanked for giving access to the NERC Hydrological Radar Experiment Dataset. We are also very grateful to USDA-ARS for providing rain gauge data from the Walnut Gulch and Riesel sites.

References

- Baldwin, M. E. and Mitchell, K. E. (1996). The NCEP hourly multi-sensor U.S. precipitation analysis. In *Preprints 11th Conf. on Numerical Weather Prediction, Norfolk, VA (USA), 19–23 August 1996*, pages J95–J96.
- Caumont, O., Ducrocq, V., Wattrelot, E., Jaubert, G., and Pradier-Vabre, S. (2010). 1D+3D-Var assimilation of radar reflectivity data: a proof of concept. *Tellus*, 62A:173–187.
- Ciach, G. J. (2003). Local Random Errors in Tipping-Bucket Rain Gauge Measurements. *J. Atmos. Ocean. Tech.*, 20:752–759.
- Cleveland, W. S. (1979). Robust Locally Weighted Regression and Smoothing Scatterplots. *J. Amer. Statist. Assoc.*, 74:829–836.
- Ducrocq, V., Ricard, D., Lafore, J.-P., and Orain, F. (2002). Storm-scale numerical rainfall prediction for five precipitating events over France: On the importance of the initial humidity field. *Weather Forecast.*, 17:1236–1256.
- Efron, B. and Tibshirani, R. (1986). Bootstrap Methods for Standard Errors, Confidence Intervals, and Other Measures of Statistical Accuracy. *Statistical Sci.*, 1:54–77.
- Fulton, R. A., Breidenbach, J. P., Seo, D. J., Miller, D. A., and O’Bannon, T. (1998). The WSR-88D rainfall algorithm. *Weather Forecast.*, 13:377–395.
- Gebremichael, M. and Krajewski, W. F. (2004). Assessment of the Statistical Characterization of Small-Scale Rainfall Variability from Radar: Analysis of TRMM Ground Validation Datasets. *J. Appl. Meteor.*, 43:1180–1199.
- Goodrich, D. C., Keefer, T. O., Unkrich, C. L., Nichols, M. H., Osborn, H. B., Stone, J. J., and Smith, J. R. (2008). Long-term precipitation database, Walnut Gulch Experimental Watershed, Arizona, United States. *Water Resour. Res.*, 44.
- Habib, E. and Krajewski, W. F. (2002). Uncertainty Analysis of the TRMM Ground-Validation Radar-Rainfall Products: Application to the TEFLUN-B Field Campaign. *J. Appl. Meteor.*, 41:558–572.
- Harmel, R. D., King, K. W., Richardson, C. W., and Williams, J. R. (2003). Long-Term Precipitation Analyses for the Central Texas Blackland Prairie. *Transactions of the ASAE*, 46:1381–1388.
- Harrison, D., Scovell, R., Lewis, H., and Matthews, S. (2006). The development of the EU-METNET OPERA radar data hub. In *Proceedings of the 4th Conf. on Radar in Meteorology and Hydrology (ERAD), Barcelona, 18-22 September 2006*, pages 388–391. Available at <http://www.crahi.upc.edu/ERAD2006/index.php>.
- Holleman, I., Delobbe, L., and Zgonc, A. (2008). Update on the European Weather Radar Network. In *Proceedings of the 5th Conf. on Radar in Meteorology and Hydrology (ERAD), Helsinki, 30 June-4 July 2008*. ISSN 978-951-697-676-4, 5 pp.
- Keenan, T. D., Glasson, K., Cummings, F., Bird, T. S., Keeler, J., and Lutz, J. (1998). The BMRC/NCAR C-Band Polarimetric (C-POL) radar system. *J. Atmos. Ocean. Tech.*, 15:871–886.
- Koizumi, K., Ishikawa, Y., and Tsuyuki, T. (2005). Assimilation of precipitation data to JMA mesoscale model with four-dimensional variational method and its impact on precipitation forecasts. *Scientific Online Letters on the Atmosphere*, 1:45–48. (www.jstage.jst.go.jp/browse/sola).

- Lin, Y. and Mitchell, K. E. (2005). The NCEP Stage II/IV Hourly Precipitation Analyses: Development and Applications. In *Proceedings of the 19th AMS Conference on Hydrology, San Diego, CA (USA), 5–14 January 2005*.
- Lopez, P. (2008). Comparison of OPERA precipitation radar composites to CMORPH, SYNOP and ECMWF model data. Technical report. ECMWF Technical Memorandum No. 569, 22 pages, Available from ECMWF, Reading, UK.
- Lopez, P. (2011). Direct 4D-Var Assimilation of NCEP Stage IV Radar and Gauge Precipitation Data at ECMWF. *Mon. Weather Rev.* in press.
- Lopez, P. and Bauer, P. (2007). “1D+4D-Var” Assimilation of NCEP Stage IV Radar and Gauge Hourly Precipitation Data at ECMWF. *Mon. Weather Rev.*, 135:2506–2524.
- Macpherson, B. (2001). Operational experience with assimilation of rainfall data in the Met.Office mesoscale model. *Meteorol. Atmos. Phys.*, 76:3–8.
- Mahfouf, J.-F., Brasnett, B., and Gagnon, S. (2007). A Canadian Precipitation Analysis (CaPa) Project: Description and Preliminary Results. *Atmosphere-Ocean*, 45:1–17.
- Moore, R. J., Jones, D. A., Cox, D. R., and Isham, V. S. (2000). Design of the HYREX raingauge network. *Hydrol. Earth Syst. Sci.*, 4:523–530.
- Morrissey, M. L., Maliekal, J. A., Greene, J. S., and Wang, J. (1995). The uncertainty of simple spatial averages using rain gauge networks. *Water Resour. Res.*, 31:2011–2017.
- Shimizu, K. (1993). A Bivariate Mixed Lognormal Distribution with an Analysis of Rainfall Data. *J. Appl. Meteor.*, 32:161–171.
- Sohn, B. J., Han, H.-J., and Seo, E.-K. (2010). Validation of Satellite-Based High-Resolution Rainfall Products over the Korean Peninsula Using Data from a Dense Rain Gauge Network. *J. Appl. Meteor. Climatol.*, 49:701–714.
- Subedi, M. and Fullen, M. A. (2009). Spatial variability in precipitation within the Hilton Experimental Site, Shropshire, UK (1982-2006). *Hydrol. Process.*, 23:236–244.
- Sun, J. (2005). Initialization and Numerical Forecasting of a Supercell Storm Observed during STEPS. *Mon. Weather Rev.*, 133:793–813.
- Šalek, M., Chèze, J.-L., Handwerker, J., Delobbe, L., and Uijlenhoet, R. (2004). Radar techniques for identifying precipitation type and estimating quantity of precipitation. Technical report. Document of COST Action 717, Task WG 1-2, 51 pp., Available from http://www.smhi.se/cost717/doc/WDF_01_200407_1.pdf.
- WMO (2008). *Guide to Meteorological Instruments and Methods of Observation*. World Meteorological Organization. WMO-No.8, 681 pages, Available from WMO, Geneva, Switzerland.
- Wood, S. J., Jones, D. A., and Moore, R. J. (2000). Accuracy of rainfall measurement for scales of hydrological interest. *Hydrol. Earth Syst. Sci.*, 4:531–543.